RESEARCH ARTICLE

Ultralow-Power Piezo-Optomechanically Tuning on CMOS-Compatible Integrated Silicon-Hafnium-Oxide Platform

Jian Shen, Yuyan Fan, Zihan Xu, Liying Wu, Ying Wang, Xiuyan Li,* Xuetao Gan, Yong Zhang,* and Yikai Su*

Power consumption of photonic integrated circuits becomes a critical consideration. A new platform is proposed for ultralow-power tuning in silicon photonics via piezo-optomechanical coupling using hafnium-oxide actuators. As an example of the potential of the platform, a tunable silicon-hafnium-oxide hybrid microring, where hafnium-oxide film acts as an active optical and piezoelectric layer, is demonstrated. The hybrid microring is capable of linear bidirectional tuning with a wavelength tuning efficiency of 8.4 pm V^{-1} and a power efficiency of 0.12 nW pm^{-1}. The estimated power consumption for tuning a free spectral range (FSR) in hybrid microring is 3.07 µW per FSR. The hybrid silicon-hafnium-oxide technology with complementary metal-oxide-semiconductor (CMOS) compatibility advances the field of ultralow-power integrated photonic devices and can find applications in optical communications, computing, and spaces under cryogenic temperatures.

J. Shen, Z. Xu, Y. Zhang, Y. Su
State Key Lab of Advanced Optical Communication Systems and Networks
Department of Electronic Engineering
Shanghai Jiao Tong University
Shanghai 200240, China
E-mail: yongzhang@sjtu.edu.cn; yikaisu@sjtu.edu.cn

Y. Fan, X. Li
National Key Laboratory of Science and Technology on Micro/Nano Fabrication
Shanghai Jiao Tong University
Shanghai 200240, China
E-mail: xiuyanli@sjtu.edu.cn

Y. Fan
Department of Micro/Nano Electronics
Shanghai Jiao Tong University
Shanghai 200240, China

L. Wu, Y. Wang
Center for Advanced Electronic Materials and Devices
Shanghai Jiao Tong University
Shanghai 200240, China

X. Gan
Key Laboratory of Light Field Manipulation and Information Acquisition
Ministry of Industry and Information Technology
and Shaanxi Key Laboratory of Optical Information Technology
School of Physical Science and Technology
Northwestern Polytechnical University
Xi'an 710129, China

DOI: 10.1002/lpor.202200248

1. Introduction

Programmable optical devices in photonic integrated circuits[1,2] serve important functions in optical phased array,[3] photonic quantum information processing,[4] machine learning,[5,6] photonic matrix multiplication,[7] optical communication,[8] and other applications. The key requirements of programmable optical systems are low power consumption, large scale, and fast response.[9] Integrated silicon photonics has drawn increasing attention to meet the scalability requirement, attributed to the compatibility with complementary metal-oxide-semiconductor (CMOS) processes.[10–13] Low power consumption and fast response tuning of silicon devices are critical issues for programmable applications in integrated photonics. Thermo-optic tuning by using a metallic microheater on a silicon waveguide is a general method to change the index of silicon.[14] However, the thermo-optic tuning exhibits high power consumption (≈10 mW), low tuning speed (≈1 kHz), and large thermal crosstalk. The low power efficiency makes it incompatible with cryogenic applications for integration with superconducting detectors[15,16] and artificial atoms.[17] Electro-optic tuning based on free-carrier dispersion is another approach to fulfill the tuning requirement.[18] However, high tuning power is still required, and free-carrier absorption increases the propagation loss and degrades the device performance. Various nonlinear materials have been integrated on silicon to achieve low-power tuning, such as graphene,[19,20] lead zirconate titanate (PZT),[21] barium titanate (BaTiO$_3$),[22] lithium niobate (LiNbO$_3$),[23] and organic electro-optic materials.[24] These approaches may face the challenges of CMOS incompatibility, large optical loss, and high fabrication complexity.

More recently, by integrating aluminum nitride (AlN) piezoelectric actuators on the silicon nitride waveguides, piezoelectrically tuning with high power efficiency of 5 nW pm^{-1} is achieved.[25] The AlN stress-optical platform on Si$_3$N$_4$ photonic circuits has enabled tunable photonic devices for programmable interferometer photonic circuit,[9] acousto-optic modulation,[25] piezoelectric control of soliton microcomb,[26] and cryogenic temperature operation.[27] However, the wavelength tuning efficiency is limited to <0.8 pm V^{-1} due to the low piezoelectric coefficient

**ADVANCED
SCIENCE NEWS**

www.advancedsciencenews.com

LASER
& PHOTONICS
REVIEWS

www.lpr-journal.org

of AlN.[25,27] It is highly desirable to achieve piezoelectrically tuning with high wavelength tuning efficiency and low power consumption.

Hafnium oxide (HfO_2) thin film has been well established as a widely used high-k oxide for gate dielectrics in the semiconductor industry for more than one decade. Its fabrication is compatible with the CMOS process. Recent macroscopic studies have demonstrated that doped HfO_2 can possess room-temperature ferroelectric and piezoelectric properties, attributed to the formation of the orthorhombic $Pca2_1$ phase.[28,29] HfO_2 exhibits a large bandgap >5 eV, which is expected to be further widened with doping.[30] Thus, it may eliminate two-photon absorption and provides a transparent window from ultraviolet to mid-infrared wavelengths. Additionally, HfO_2 has a high dielectric constant, a high breakdown field of ≈3.9–6.7 MV cm^{-1}, and a low thermal conductivity, which can be used as a spacer layer.[31]

In this work, we develop a hybrid integrated silicon-HfO_2 photonic platform using HfO_2 thin films as both a piezoelectric layer and a light guiding medium. The fabrication process is compatible with current CMOS technology. 20 nm thick Zr doped HfO_2 thin film is introduced as a piezoelectric material using the atomic layer deposition (ALD) method benefiting from its significant second-order nonlinearity, mature deposition technology, and compatibility with silicon substrate. To increase the optical field in the ultrathin and low-index doped HfO_2 layer, we design a horizontal slot waveguide structure to sandwich the low-index doped HfO_2 layer between two high-index silicon layers. To demonstrate the piezoelectric effect of the doped HfO_2 film, we fabricate and measure electrically tunable microring resonators based on the slot waveguide geometry. The hybrid microring resonator is capable of linear bidirectional tuning with a wavelength tuning efficiency of 8.4 pm V^{-1} and a power efficiency of 0.12 nW pm^{-1}. The estimated power consumption of hybrid microring is 3.07 μW per FSR. The proposed CMOS-compatible Si-HfO_2 piezo-optomechanical approach offers comparable power efficiency and one order of magnitude improvement in tuning efficiency relative to that of Si_3N_4 devices actuated by AlN[9,25–27] and three orders of magnitude reduction in power consumption compared to that of conventional thermo-optic tuning approach.[32] Our demonstration of doped HfO_2 as an active optical and piezoelectric layer monolithically integrated on silicon opens new avenues toward the application of CMOS-compatible piezo-actuators in fully integrated silicon photonic circuits.

2. Device Design and Operation Principle

The proposed Si-HfO_2 platform consists of silicon layers and 20 nm thick Zr doped HfO_2 ($Hf_{0.5}Zr_{0.5}O_2$, HZO) thin film. HZO has a low refractive index ($n_{HZO} = 1.8$, $n_{Si} = 3.467$ at 1.55 μm).[33] The optical field is mostly confined in the high-index silicon layer for a conventional rib waveguide structure. To increase the optical field in the thin HZO film and the piezo-electrically tuning efficiency, we design a horizontal slot waveguide consisting of the low-index HZO film sandwiched between the two high-index silicon layers, as shown in **Figure 1**. The 100 nm thick top silicon layer of a silicon-on-insulator (SOI) wafer is the lower Si layer of the slot waveguide, while a 100 nm thick amorphous silicon (a-Si) layer is used as the upper layer of the horizontal slot. The patterns

of waveguides, gratings, and microrings are defined on the a-Si layer. We use the finite element method to simulate the mode properties of the hybrid waveguide. The effective mode index of the 2 μm wide slot waveguide is calculated to be $n_{eff} = 1.453$. The light confinement in the 20 nm thick HZO film is $\Gamma_{HZO} \approx 17.4\%$ for the transverse magnetic (TM) slot waveguide mode. The confinement factor can reach >55 % by optimizing the waveguide width and increasing the HZO thickness to 80 nm, as shown in Figure 1b. As illustrated in Figure 1b,c, the effective refractive index increases when the thicknesses of the HZO layer and the upper a-Si layer increase. Furthermore, the width variation of the horizontal slot waveguide shows a small impact on the light confinement factor and the effective index, as depicted in Figure 1d.

To exploit the piezo-optomechanical effect of the hybrid waveguide, we apply the electric field through planar microelectrodes beside the waveguide, as shown in **Figure 2**a. The simulated static electric field distribution is plotted in Figure 2b when a bias voltage of 10 V is applied to the electrodes. The simulation suggests that the average electric field E_{avg} inside the hybrid waveguide increases as the gap between the electrode and the waveguide becomes smaller (Figure 2c). The metal absorption of the gold electrodes is negligible due to the strong optical confinement of the hybrid slot waveguide. The overlap between the optical and electrical fields is important to increase the modulation efficiency, which can be quantified by the electro-optic integral. The electro-optic integral Γ is[34]

$$\Gamma = \frac{g}{V} \frac{\int\int E_{x,op}^2 E_e dx dz}{\int\int E_{x,op}^2 dx dz} \tag{1}$$

where g is the electrode separation, V is the voltage on the electrodes, $E_{x,op}$ is the optical field, and E_e is the electrical field. Figure 2d plots simulated Γ as a function of the HZO thicknesses for different a-Si thicknesses. It indicates that electro-optic integral Γ increases as the HZO thickness increases and the a-Si thickness decreases. In the experiment, the HZO thickness is 20 nm to ensure the high yield of the deposited HZO film.

When applying the electric field, the refractive index modulation is achieved by piezo-optomechanical coupling due to the strain-optic effect and moving boundary effect.[35] The strain generated by the piezoelectric response in the HZO film introduces a photoelastic refractive index shift in the HZO and Si layers. On the other hand, the displacement of the film boundaries induces the change of the effective mode index.

For a microring resonator, the resonance condition is

$$Ln_{eff} = m\lambda \tag{2}$$

where L is the round-trip ring length, n_{eff} is the effective mode index, λ is the resonance wavelength, m is the longitudinal mode number. The piezo-electric induced strain imparts resonance change $\Delta\lambda$ to the optical mode

$$\Delta\lambda = \Delta n_{eff}L + n_{eff}\Delta L \tag{3}$$

where Δn_{eff} is the strain-induced index change, ΔL is the strain-induced length change of the microring. The strain-induced index change consists of the contributions from the strain-optic
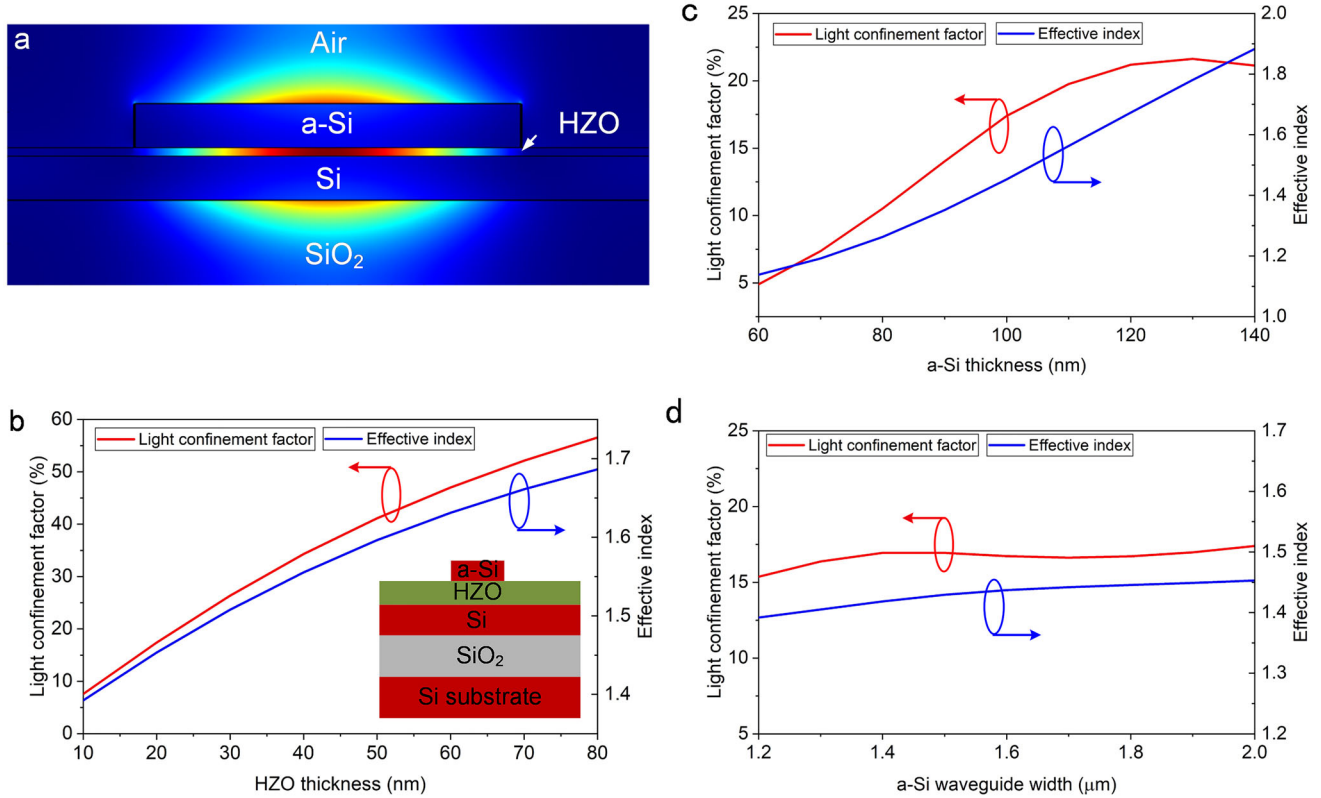
ADVANCED
SCIENCE NEWS

www.advancedsciencenews.com

LASER
& PHOTONICS
REVIEWS

www.lpr-journal.org

Figure 1. a) Simulated mode profile of the proposed Si-HfO$_2$ hybrid waveguide. b) Numerically calculated light confinement factor and effective index as a function of the HZO thickness. Inset: cross-section of the Si-HfO$_2$ hybrid waveguide. c) Calculated light confinement factor and effective index as a function of the upper a-Si layer thickness. d) Calculated light confinement factor and effective index as a function of the waveguide width.

($\Delta n_{\text{eff,s}}$) effect and moving boundary ($\Delta n_{\text{eff,b}}$) effect, and can be expressed as

$$\Delta n_{\text{eff}} = \Delta n_{\text{eff,s}} + \Delta n_{\text{eff,b}} \tag{4}$$

The strain-optic induced index change $\Delta n_{\text{eff,s}}$ is related to the optomechanical resulting stress. Since the waveguide is usually very long in the propagation direction z, the strain and the index change in this axis are negligible. Thus the expression between the strain-optic induced index change Δn and stress σ is given by[36]

$$\Delta n_x = -C_1\sigma_x - C_2(\sigma_y + \sigma_z) \tag{5}$$

$$\Delta n_y = -C_1\sigma_y - C_2(\sigma_z + \sigma_x) \tag{6}$$

where σ_x, σ_y, and σ_z are the stress tensor components along the x, y, and z directions, Δn_x and Δn_y denote the strain-optic induced index change in the x and y directions, respectively. The stress-optic coefficients C_1 and C_2 depend on the material refractive index without stress (n_0), Young's modulus (E), Poisson's ratio (v), and the photoelastic tensor elements (p_{11} and p_{12}) as[36]

$$C_1 = \frac{n_0^3}{2E}(p_{11} - 2vp_{12}) \tag{7}$$

$$C_2 = \frac{n_0^3}{2E}(-vp_{11} + (1-v)p_{12}) \tag{8}$$

We estimate the strain values and deformation in the HZO and Si layers from a finite element model using approximate values of HZO piezoelectric coupling coefficients, waveguide geometries, and material constants, as shown in Figure 2e. The photo-elastic coefficients of Si used in our model are $p_{11} = -0.101$, $p_{12} = 0.0094$. The photoelastic coefficients of HZO are $p_{11} = 0.3865$, $p_{12} = 0.2538$.[37] The piezoelectric coefficients $e_{31,f}$ and $e_{33,f}$ used in the model are -3.3 and 5.739 C m^{-2}, which are examined by exploiting thermal expansion of the substrate upon rapid temperature cycling[38] and measured via double beam laser interferometry (DBLI),[39] respectively. The detailed material constants of HZO film used in the model are provided in the Supporting Information 1. The calculated Von Mises stress value in the horizontal (x) direction is 12 MPa when the applied potential difference is 10 V. Using the simulated stress values and Equations (2)–(8), the calculated wavelength tuning efficiency is 2.97 pm V^{-1}. The wavelength tuning efficiency is much larger than that of reported Si$_3$N$_4$ devices actuated by AlN.[27] We attribute that to the larger piezoelectric coefficient of HZO films and the coupled nature of the piezoelectric actuator and optical waveguide of the platform.

3. Device Fabrication and Characterization

The fabrication process for preparing Si-HfO$_2$ monolithically integrated devices is illustrated as follows. 20 nm thick Hf$_{0.5}$Zr$_{0.5}$O$_2$ film is deposited at 300 °C on an SOI substrate with a top silicon layer of 100 nm and a buried oxide layer of 1.1 μm using
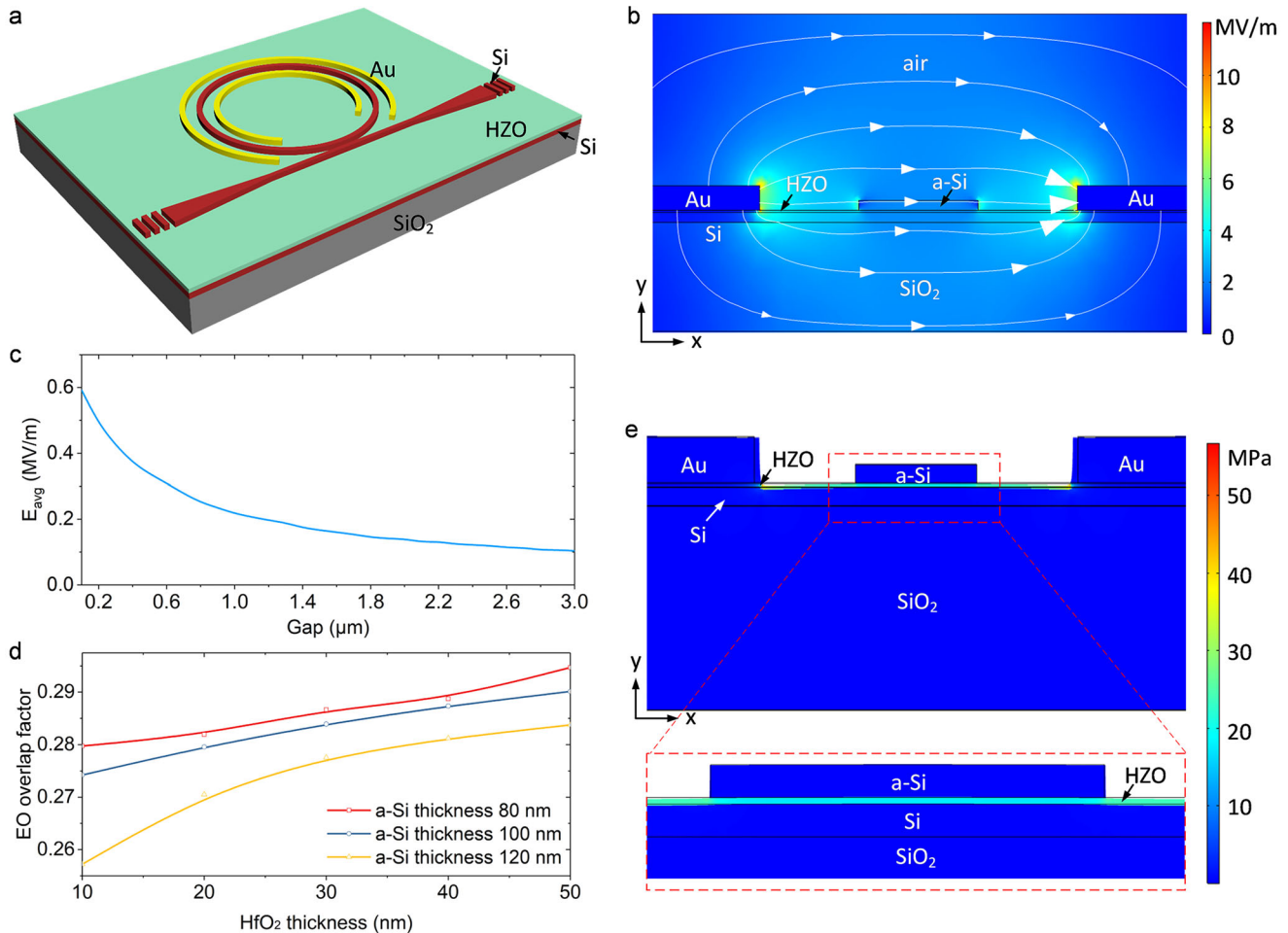
Figure 2. a) Integrated piezo-optomechanical tunable microring based on Si-HfO$_2$ platform. b) Simulated static electric field distribution of the Si-HfO$_2$ hybrid waveguide induced by the planar electrodes. c) Simulated average electric field E_{avg} inside the hybrid waveguide as a function of the gap between the electrode and the waveguide. d) Numerically calculated electro-optic overlap integral Γ as a function of HZO and a-Si thicknesses. The gap between the electrode and the waveguide is 2 μm and the applied voltage is 1 V. e) Finite element analysis of the Von Mises stress and deformation from an applied potential difference of 10 V to the hybrid waveguide. Deformation is scaled by 10 000x for visibility.

the ALD method (Beneq thermal-/plasma-enhanced ALD). Tetrakis-ethylmethylamino-hafnium (TEMAHf) and tetrakis-ethylmethylamino-zirconium (TEMAZr) are used as precursors and ozone is used as oxidant. The concentration ratio of Hf to Zr is controlled by the number ratio of the growth cycle. Post-deposition annealing (PDA) is carried out at 650 °C for 30 s in flowing N$_2$. The atomic force micrograph (AFM) on the surface and grazing-angle incidence X-ray diffraction (GIXRD) scanning spectrum of the HZO film are shown in **Figure 3**a,c. The HZO surface has a root-mean-square (RMS) roughness of 1.56 nm. Three diffraction peaks belong to orthorhombic or tetragonal or cubic (O/T/C) and phases monoclinic (M) are presented at 30.5°, 28.5°, and 31.6°, respectively, as shown in Figure 3c. As reported in ref. [29] optimized ferroelectricity is observed with the presented ratio of O/T/C phase. We characterize the C–V curve and polarization hysteresis loop of the HZO thin film to show its ferroelectric property. The HZO film is deposited on the doped silicon substrate using the same deposition condition by ALD. The doped silicon substrate is used as the bottom electrodes, and

the upper gold electrodes are formed on the HZO thin film by thermal evaporation process. The C–V curve is measured by the impedance analyzer (Keysight E4990A), as shown in Figure 3d. The inset of Figure 3d shows the schematic of the device structure and experimental setup. The measured C–V characteristic is observed with coercive voltages at 3.6 and −2 V. The difference between the positive and negative coercive voltages in the C–V curve may be attributed to the asymmetry of the electrodes.[30]

Furthermore, the polarization hysteresis loop is obtained by electrical polarization measurement (Keithley 4200). The polarization intensity is calculated by the electrode area of 37 206.3 μm^2. The measurements are performed at room temperature. The 1 and 10 kHz triangular wave signals are employed, respectively. For the ferroelectric material, domain flipping accompanied by the movement of the domain walls occurs when the polarization of the domain aligns with the applied electrical field along the polarization axis.[40,41] In the measurement, as the applied voltage increases, the number of the domain flipping along the polarization axis increases. The maximum number of the
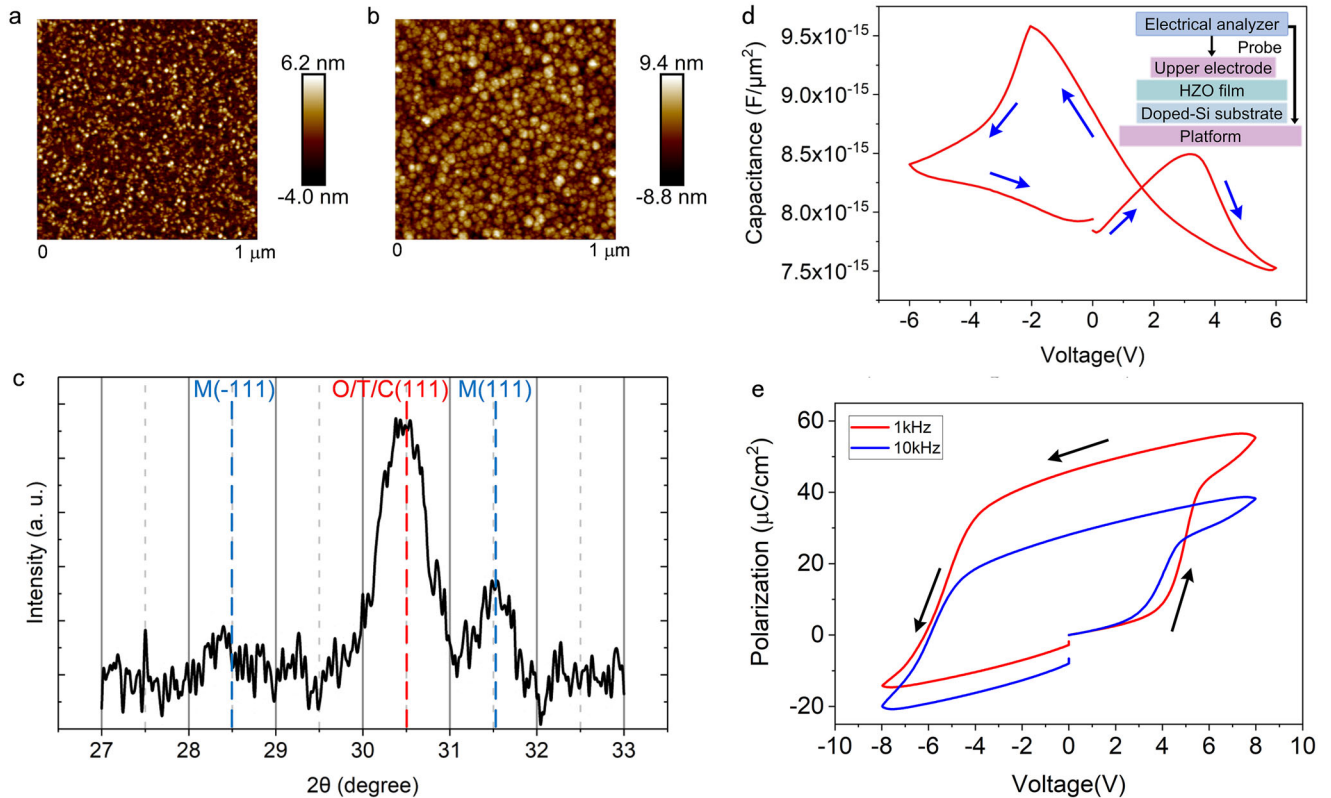
2200248 (4 of 10)

**ADVANCED
SCIENCE NEWS**

www.advancedsciencenews.com

**LASER
& PHOTONICS
REVIEWS**

www.lpr-journal.org

Figure 3. AFM on the surface of a) the HZO film and b) the a-Si film. c) GIXRD scanning spectrum of the HZO film. d) Measured C–V curve of the HZO thin film. Inset: Schematic of the device structure and experimental setup. e) Measured polarization hysteresis loop of the HZO thin film.

domain flipping can be reached near the coercivity voltage of ≈5 and −5 V, as illustrated in Figure 3e.

Then, 100 nm thick a-Si film is deposited at a temperature of 300 °C by plasma-enhanced chemical vapor deposition (PECVD). The AFM on the surface of the a-Si film is shown in Figure 3b. The RMS roughness is 2.65 nm. The patterns consisting of grating couplers, microrings, and waveguides are defined on the resist (AR-P 6200.09) and transferred to the a-Si layer by electron-beam lithography (EBL, Vistec EBPG 5200+) and inductively coupled plasma (ICP) dry etching (SPTS DRIE-I). Finally, 250 nm thick Au electrodes and contact pads are fabricated using electron beam evaporation and patterned by the lift-off process. The flow chart of the fabrication process is provided in the Supporting Information 1.

4. Measurement and Results

To characterize the loss of the Si-HfO$_2$ slot waveguide, we fabricate microring resonators with a radius of 100 µm, a width of 1.6 µm, and different coupling gaps from 40 to 140 nm. By varying the gap between the access waveguide and the ring, the coupling condition can be tuned to obtain critical coupling with a high extinction ratio. The devices are characterized by using a tunable laser scanning system (EXFO T100S-HP-CLU-M-CTP10-00). On-chip grating couplers are used to couple light into/out of the Si-HfO$_2$ slot waveguides (the Supporting Information 1, Section 3). **Figure 4** shows the micrographs and transmission spec-

tra of the fabricated Si-HfO$_2$ slot microring resonator. The loaded quality factor Q, free-spectral range (FSR), and extinction ratio are 7700, 0.96 nm, and 24 dB, respectively. The propagation loss of the slot waveguide is expressed as

$$\alpha = \frac{2\pi n_{\mathrm{g}}}{Q_{\mathrm{int}}\lambda_0} = \frac{\lambda_0}{Q_{\mathrm{int}} \cdot R \cdot FSR} \tag{9}$$

where α is the loss per unit length, R is the radius of the ring, Q_{int} is the intrinsic quality factor. The propagation loss of the fabricated Si-HfO$_2$ slot waveguide is estimated to be 11.1 cm^{-1}. The pure a-Si racetrack resonators without the HZO film are fabricated on the SOI substrate by the same process (see the Supporting Information 1, Section 4). The propagation loss of the fabricated a-Si on Si waveguide is estimated as 4.5 cm^{-1}. The estimated loss purely on the HZO film is 6.6 cm^{-1}. The relatively large loss may be attributed to the roughness of the HZO film and the high deposition temperature of the a-Si film. The thermal desorption of hydrogen occurs above 250 °C, increasing the defect density of a-Si film.[42] In addition, the top surface of the a-Si layer is approximately six times as rough as that of the commercial SOI wafer, leading to large propagation loss. It is expected to reduce the propagation loss by depositing a-Si film at a process temperature of 250 °C and smoothing the top surface by chemical mechanical polishing (CMP) process.

To demonstrate the ultralow-power piezo-optomechanically tuning of our platform, microrings with gold microelectrodes
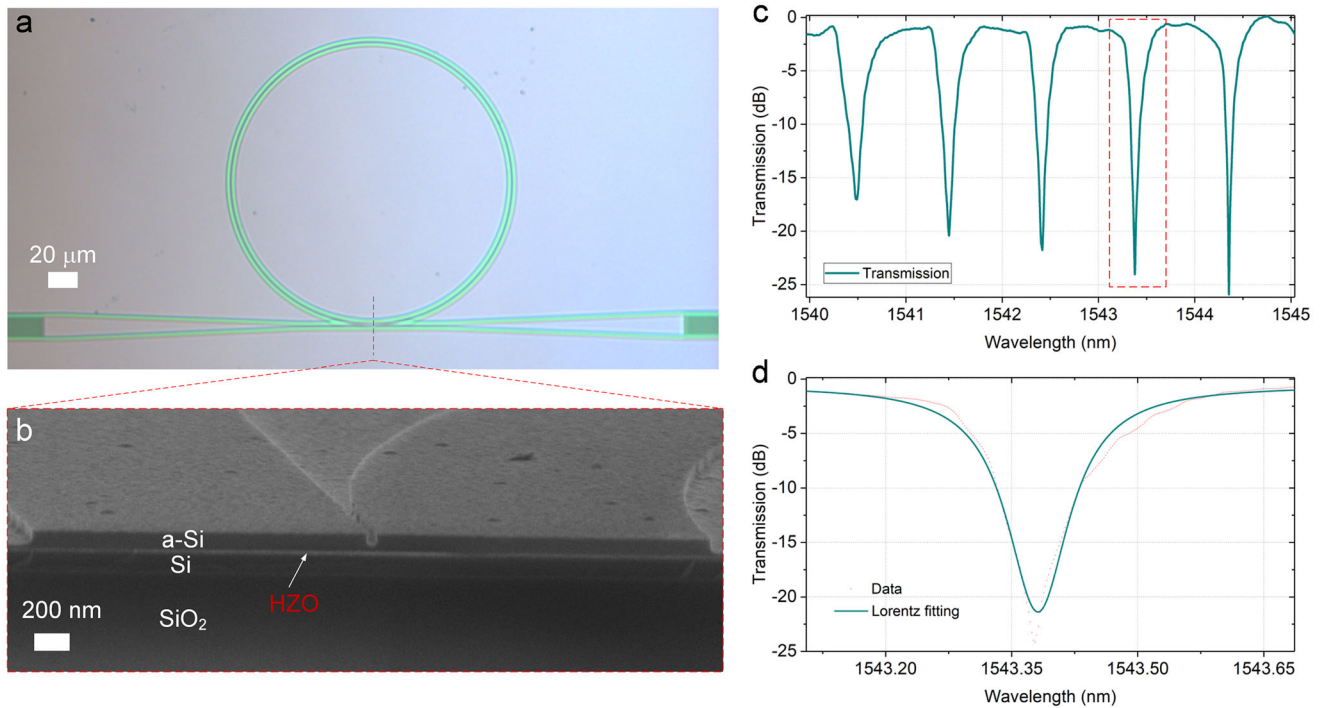
Figure 4. Results of fabricated Si-HfO$_2$ slot microring. a) Optical microscope graph of fabricated microring. b) Scanning electron microscope (SEM) cross-sectional photo of the coupling region between access waveguide and ring. c) Measured transmission spectrum of the slot microring. d) Zoomed spectrum and Lorentz fitting of a resonance dip.

are fabricated and characterized. **Figure 5**a–c plots optical microscope and SEM photos of a tunable microring, showing the electrical and optical routing to the ring. The separation between the ring and the electrode is 2 μm. Due to the large propagation loss and strong optical field confinement capability of TM slot waveguide mode, a smaller coupling gap is required to satisfy the critical coupling condition. The ring has a radius of 70 μm, a width of 1.2 μm, and a coupling gap of 50 nm. Figure 5d illustrates the stress-optic tuning of the resonances. Upon applying an electric field across the ring, the resonance wavelengths shift, indicating a change in the effective index of the ring. To verify that the device works fine at high voltages, the finite element method is used to simulate the electric field distribution of the device with planar microelectrodes beside the waveguide (see the Supporting Information 1, Section 5). From the simulated results, the applied voltage in our experiment does not cause a dielectric breakdown. The average linear tuning efficiency is $\Delta\lambda/\Delta V = 8.4$ pm V^{-1}, as shown in Figure 5e. We consider that the difference in the tuning efficiency between calculation and experiment is mainly related to the material constants of HZO film, especially the piezoelectric coefficient. The growth conditions, doping, and thickness of the HZO film differ from those of refs. [38, 39], which results in the different piezoelectric coefficients $e_{33,f}$ of the HZO film. The half-wave voltage-length product is estimated to be $V_\pi L = L\cdot\text{FSR}\cdot\Delta V/(2\cdot\Delta\lambda) \approx 3.24$ V$_{\text{cm}}$.[21] The tuning efficiency is one order of magnitude improvement compared to that of AlN-actuated Si$_3$N$_4$ devices,[27] which is attributed to the larger piezoelectric coefficient of HZO and the coupled nature of the piezoelectric actuation and optical waveguide of the platform. The hysteresis effect of the resonance wavelength shifts is measured by cycling the ap-

plied voltage in another Si-HZO microring device on the same chip. The differences in the hysteresis curves between different devices on the same chip may be related to the growth quality and uniformity of the HZO thin film (see the Supporting Information 1, Section 6). In contrast to the unidirectional tuning using thermo-optic heaters, the piezo-optomechanically tuning is bidirectional. This is attributed to the signed strain-induced index change depending on the direction of the strain. When the direction of the applied electrical field is reversed, an opposite-change of the index is introduced, leading to the opposite-directional tuning. A linear phase shifter with a single-drive push-pull or differential configuration is expected to be implemented, benefiting from the bidirectional tuning. To exclude a possible contribution of plasma dispersion induced by the strong electric field in the silicon, the racetrack resonators without the HZO layer are fabricated and characterized. No resonance shifting is observed in the a-Si devices without HZO thin films. It indicates that the resonance shift of the Si-HZO devices can be fully attributed to the piezo-optomechanical effect in the HZO layer (see the Supporting Information 1, Section 4).

Leakage current across the Si-HfO$_2$ microring is measured by a semiconductor parameter analyzer (Agilent BA1500). In the measurement, power line cycle (PLC) mode in the high-resolution analog-to-digital converter (ADC) is utilized. Under the PLC mode, the integration time can be calculated as 20 ms. This integration time allows for accurate measurement of the hysteretic characteristics of the device.[43,44] To rule out the artifact on the hysteretic behavior caused by the source monitor unit (SMU), the leakage current of the bare a-Si on Si racetrack resonator is measured using the same test conditions. As depicted
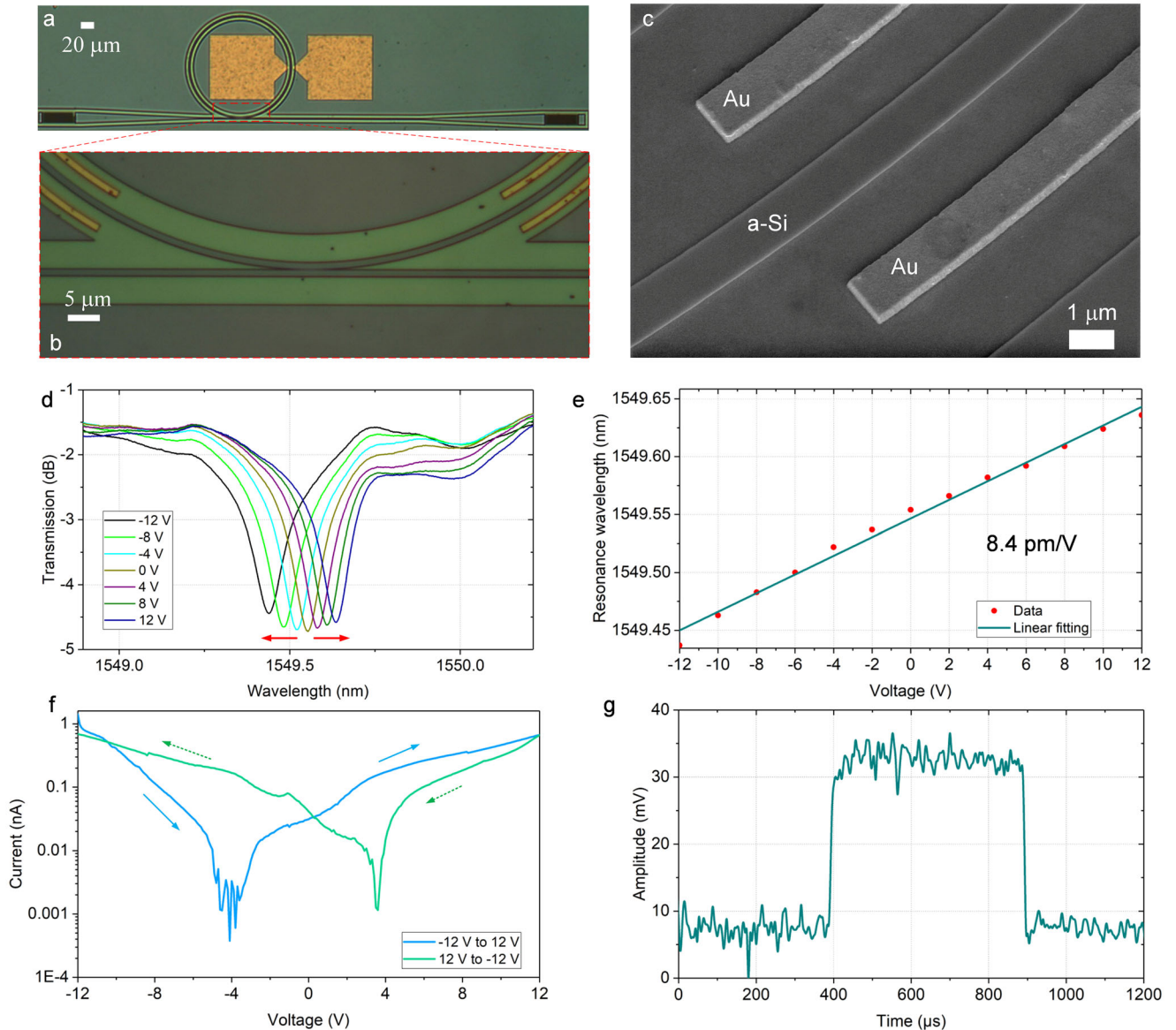
ADVANCED
SCIENCE NEWS

www.advancedsciencenews.com

LASER
& PHOTONICS
REVIEWS

www.lpr-journal.org

Figure 5. a) Optical microscope image of fabricated hybrid microring with gold electrodes. b) Magnified photo for coupling region of the microring. c) SEM photo of the ring waveguide and electrodes. d) Measured transmission spectra of fabricated microring upon applying different voltages. e) Stress-optic tuning of the resonances versus applied voltages. f) Measured I–V hysteresis curve of the microring. g) Temporal response of the microring.

in Figure S5d (Supporting Information), no hysteresis behavior is observed in the I–V curve for the a-Si on Si racetrack. It indicates that the hysteretic behavior of the I–V curve for Si-HZO devices is attributed to the ferroelectric property of the HZO thin film.

Figure 5f shows the measured I–V hysteresis curve of the Si-HfO_2 microring. During the measurements, a bias voltage is applied between the electrodes and swept, which causes the resistive change due to the sweep direction of the voltage in bipolar-type resistive switching: minimum voltage → maximum voltage → minimum voltage. The bump of the I–V curve at around 3.8/−3.8 V indicates the ferroelectric behavior. From the measured C–V characteristic, the coercive voltages at 3.6 and −2 V are observed, as shown in Figure 3d. Both of them illustrate

the presence of ferroelectric property in the HZO thin film. The slight difference in the coercive voltages between the I–V and C–V curves is attributed to the different electrode structures in the two tests. The hysteretic curve is attributed to the wake-up effect of the doped HfO_2 ferroelectric films, which is caused by the redistribution of defects, especially oxygen vacancies in the films.[45] Since the HZO actuator is capacitive, the current is measured to be less than 1 nA when the voltage is swept from −12 to 12 V. The resonance shift induced by the voltages of −12 to 12 V is 200 pm, thus, the power efficiency is estimated to be 0.12 nW pm^{-1}. The measured power efficiency is comparable with that of AlN-actuated Si_3N_4 microrings,[25] three to four orders of magnitude improvement as that of thermo-optic approach[32] and PZT-actuated Si_3N_4 microring.[35] The power consumption of Si-HfO_2

Table 1. Performance of various state-of-the-art integrated tunable devices.

Structures and materials	Tuning mechanism	Tuning efficiency [pm V^{-1}]	Power efficiency [nW pm^{-1}]	Power consumption [μW per FSR]	CMOS compatibility
Suspended silicon racetrack[32]	Thermo-optic	/	208	2400	Yes
Silicon ring[46]	Plasma dispersion in Si	/	92	>500	Yes
Silicon nitride ring on BaTiO$_3$[22]	Pockels effect	25	0.0424	0.106	No
PZT on silicon nitride ring[35]	Piezo-optomechanically	≈25	1200	500	No
PZT on silicon ring[47]	Piezo-optomechanically	≈19	/	/	No
Silicon nitride ring on AlN[27]	Piezo-optomechanically	0.8	0.0125	/	Yes
AlN on silicon nitride ring[25]	Piezo-optomechanically	≈0.125–0.2	5	/	Yes
Si-HfO$_2$ ring This work	Piezo-optomechanically	8.4	0.12	3.07	Yes

microring is estimated to be 3.07 μW per FSR (see the Supporting Information 1, Section 7), which are two to three orders of magnitude less than that in plasma dispersion- and thermo-optic-based silicon tunable devices.

We also measure the tuning speed for the Si-HfO$_2$ tunable microring by driving the electrodes with a 2 kHz square-wave voltage signal. Figure 5g shows the measured response for the device. The ≈10–90% switching times are 15 and 8 μs for the rising edge and the falling edge, respectively. However, the high and low levels of the output signal can no longer be distinguished on the sampling oscilloscope when a 1 MHz square wave signal is applied to the device. To demonstrate the high-speed response of the Si-HZO devices, we apply the sinusoidal signals of different frequencies to the on-chip device (see the Supporting Information 1, Section 8). From the measured results, the poor high-speed performance may be related to the mechanical design of the Si-HZO actuator.[9,25,27]

Table 1 compares the performance of our Si-HfO$_2$ microrings with some state-of-the-art silicon integrated tunable devices. For traditional tunable devices based on thermo-optic and plasma dispersion effects, the power efficiency is low and at the order of 100 nW pm^{-1}. For BaTiO$_3$-Si or PZT-Si hybrid devices, large tuning efficiency and high power efficiency can be achieved. However, the devices are not compatible with the CMOS process. CMOS-compatible AlN-actuated Si$_3$N$_4$ devices have made significant progress in recent years. Unfortunately, the tuning efficiency is low and at the order of 0.1 pm V^{-1} due to the low piezoelectric coefficient of AlN and weak coupling between the piezoelectric actuator and the optical waveguide. The proposed Si-HfO$_2$ hybrid platform based on piezo-optomechanical tuning exhibits large tuning efficiency, high power efficiency, and CMOS compatibility, where doped HfO$_2$ thin film acts as both a piezoelectric layer and a light guiding medium.

5. Conclusion and Discussion

We have presented a CMOS-compatible piezo-optomechanically tuning approach on an integrated silicon-hafnium-oxide platform. In a proof-of-concept demonstration, we have fabricated a tunable hybrid microring actuated by doped HfO$_2$ film. Unlike the weak coupling of the piezoelectric actuation layer and optical guiding layer in previous AlN-actuated Si$_3$N$_4$

microrings,[25–27] the doped HfO$_2$ film acts as both piezoelectric actuator and optical waveguide in the new platform. The new piezo-optomechanical approach offers one order of magnitude improvement in tuning efficiency.

The presented device shows great promise for the applications of piezoactuators in fully integrated silicon photonic circuits, while there are some improvements needed for future work. First, the propagation loss of the fabricated hybrid Si-HfO$_2$ waveguide is relatively high. The optimization of the deposition condition for HZO and a-Si film and the CMP process can be used to reduce the defect density and the roughness, leading to an expected propagation loss of sub-1 dB cm^{-1}.[42] Second, the doped HfO$_2$ thin film can be monolithically integrated on silicon nitride to achieve waveguides with ultralow-loss of sub-1 dB cm^{-1} in the future, benefiting from ultralow loss property of silicon nitride material.[26] Third, the thickness of piezoelectric HZO film is only 20 nm. Higher optical confinement factor and larger electro-optic overlap factor can be achieved in thicker HZO film, which is expected to realize larger tuning efficiency. Finally, a full FSR of tuning is not achieved in fabricated hybrid devices. However, the tuning range could be significantly increased for a larger electric field. The use of transparent conducting electrodes (indium tin oxide, ITO)[48] and a smaller electrodes gap can enable a larger electric field.

In addition to the compact tunable microring devices, linear phase shifters with much longer piezoactuation waveguide length can be constructed on the Si-HfO$_2$ platform, enabling low-bias operation. A push-pull or differential configuration can be also used in the phase shifter, then, applied electric fields induce phase shifts with an equal magnitude but opposite sign in the two arms, leading to a half operation bias. The calculations indicate $V_\pi = 5.4$ V for a 3 mm long push-pull linear phase shifter based on the Si-HfO$_2$ platform. Broadband optical switches[18] and programmable Mach–Zehnder meshes[1,2] with ultralow power consumption are expected to be achieved using the Si-HfO$_2$ linear phase shifters.

The approach of hybrid Si-HfO$_2$ waveguides extends the toolbox of CMOS-compatible silicon photonics technology. It can be used to realize ultralow-power switching and tuning and find applications in optical communication, photonic quantum information processing, control of soliton microcombs, optical phased array, and spaces under cryogenic temperatures.

Conflict of Interest

The authors declare no conflict of interest.

Data Availability Statement

The data that support the findings of this study are available from the corresponding author upon reasonable request.

[1] W. Bogaerts, D. Pérez, J. Capmany, D. A. B. Miller, J. Poon, D. Englund, F. Morichetti, A. Melloni, *Nature* **2020**, *586*, 207.

[2] N. C. Harris, J. Carolan, D. Bunandar, M. Prabhu, M. Hochberg, T. Baehr-Jones, M. L. Fanto, A. M. Smith, C. C. Tison, P. M. Alsing, D. Englund, *Optica* **2018**, *5*, 1623.

[3] J. Sun, E. Timurdogan, A. Yaacobi, E. S. Hosseini, M. R. Watts, *Nature* **2013**, *493*, 195.

[4] K. K. Mehta, C. D. Bruzewicz, R. McConnell, R. J. Ram, J. M. Sage, J. Chiaverini, *Nat. Nanotechnol.* **2016**, *11*, 1066.

[5] G. Wetzstein, A. Ozcan, S. Gigan, S. Fan, D. Englund, M. Soljačić, C. Denz, D. A. B. Miller, D. Psaltis, *Nature* **2020**, *588*, 39.

[6] M. Prabhu, C. Roques-Carmes, Y. Shen, N. Harris, L. Jing, J. Carolan, R. Hamerly, T. Baehr-Jones, M. Hochberg, V. Čeperić, J. D. Joannopoulos, D. R. Englund, M. Soljačić, *Optica* **2020**, *7*, 551.

[7] H. Zhou, J. Dong, J. Cheng, W. Dong, C. Huang, Y. Shen, Q. Zhang, M. Gu, C. Qian, H. Chen, Z. Ruan, X. Zhang, *Light: Sci. Appl.* **2022**, *11*, 30.

[8] R. Soref, *APL Photonics* **2018**, *3*, 021101.

[9] M. Dong, G. Clark, A. J. Leenheer, M. Zimmermann, D. Dominguez, A. J. Menssen, D. Heim, G. Gilbert, D. Englund, M. Eichenfield, *Nat. Photonics* **2022**, *16*, 59.

[10] Y. He, Y. Zhang, Q. Zhu, S. An, R. Cao, X. Guo, C. Qiu, Y. Su, *J. Lightwave Technol.* **2018**, *36*, 5746.

[11] Y. Su, Y. Zhang, C. Qiu, X. Guo, L. Sun, *Adv. Mater. Technol.* **2020**, *5*, 1901153.

[12] Y. Zhang, Y. He, H. Wang, L. Sun, Y. Su, *ACS Photonics* **2021**, *8*, 202.

[13] H. Wang, L. Sun, Y. He, G. Tang, S. An, Z. Wang, Y. Du, Y. Zhang, L. Yuan, X. He, J. Dong, Y. Su, *Laser Photonics Rev.* **2022**, *16*, 2100631.

[14] Y. Zhang, Y. He, Q. Zhu, X. Guo, C. Qiu, Y. Su, R. Soref, *Opt. Lett.* **2018**, *43*, 4518.

[15] F. Najafi, J. Mower, N. C. Harris, F. Bellei, A. Dane, C. Lee, X. Hu, P. Kharel, F. Marsili, S. Assefa, K. K. Berggren, D. Englund, *Nat. Commun.* **2015**, *6*, 5873.

[16] X. Zheng, P. Zhang, R. Ge, L. Lu, G. He, Q. Chen, F. Qu, L. Zhang, X. Cai, Y. Lu, S. Zhu, P. Wu, X. Ma, *Adv. Photonics* **2021**, *3*, 055002.

[17] N. H. Wan, T.-J. Lu, K. C. Chen, M. P. Walsh, M. E. Trusheim, L. De Santis, E. A. Bersin, I. B. Harris, S. L. Mouradian, I. R. Christen, E. S. Bielejec, D. Englund, *Nature* **2020**, *583*, 226.

[18] L. Lu, S. Zhao, L. Zhou, D. Li, Z. Li, M. Wang, X. Li, J. Chen, *Opt. Express* **2016**, *24*, 9295.

[19] D. Akinwande, C. Huyghebaert, C.-H. Wang, M. I. Serna, S. Goossens, L.-J. Li, H. S. P. Wong, F. H. L. Koppens, *Nature* **2019**, *573*, 507.

[20] X. Gan, R.-J. Shiue, Y. Gao, I. Meric, T. F. Heinz, K. Shepard, J. Hone, S. Assefa, D. Englund, *Nat. Photonics* **2013**, *7*, 883.

[21] K. Alexander, J. P. George, J. Verbist, K. Neyts, B. Kuyken, D. Van Thourhout, J. Beeckman, *Nat. Commun.* **2018**, *9*, 3444.

[22] J. E. Ortmann, F. Eltes, D. Caimi, N. Meier, A. A. Demkov, L. Czornomaz, J. Fompeyrine, S. Abel, *ACS Photonics* **2019**, *6*, 2677.

[23] J. Chiles, S. Fathpour, *Optica* **2014**, *1*, 350.

[24] C. Kieninger, Y. Kutuvantivida, D. L. Elder, S. Wolf, H. Zwickel, M. Blaicher, J. N. Kemal, M. Lauermann, S. Randel, W. Freude, L. R. Dalton, C. Koos, *Optica* **2018**, *5*, 739.

[25] H. Tian, J. Liu, B. Dong, J. C. Skehan, M. Zervas, T. J. Kippenberg, S. A. Bhave, *Nat. Commun.* **2020**, *11*, 3073.

[26] J. Liu, H. Tian, E. Lucas, A. S. Raja, G. Lihachev, R. N. Wang, J. He, T. Liu, M. H. Anderson, W. Weng, S. A. Bhave, T. J. Kippenberg, *Nature* **2020**, *583*, 385.

[27] P. R. Stanfield, A. J. Leenheer, C. P. Michael, R. Sims, M. Eichenfield, *Opt. Express* **2019**, *27*, 28588.

[28] D. Martin, J. Müller, T. Schenk, T. M. Arruda, A. Kumar, E. Strelcov, E. Yurchuk, S. Müller, D. Pohl, U. Schröder, S. V. Kalinin, T. Mikolajick, *Adv. Mater.* **2014**, *26*, 8198.

[29] T. Mittmann, M. Materano, P. D. Lomenzo, M. H. Park, I. Stolichnov, M. Cavalieri, C. Zhou, C.-C. Chung, J. L. Jones, T. Szyjka, M. Müller, A. Kersch, T. Mikolajick, U. Schroeder, *Adv. Mater. Interfaces* **2019**, *6*, 1900042.

[30] J. Qin, F. Huang, X. Li, L. Deng, T. Kang, A. Markov, F. Yue, Y. Chen, X. Wen, S. Liu, Q. Xiong, S. Semin, T. Rasing, D. Modotto, R. Morandotti, J. Xu, H. Duan, L. Bi, *ACS Nano* **2019**, *13*, 1213.

[31] W.-C. Hsu, C. Zhen, A. X. Wang, *ACS Photonics* **2021**, *8*, 1933.

[32] P. Dong, W. Qian, H. Liang, R. Shafiiha, D. Feng, G. Li, J. E. Cunningham, A. V. Krishnamoorthy, M. Asghari, *Opt. Express* **2010**, *18*, 20298.

[33] H. C. Shin, D. Tahir, S. Seo, Y. R. Denny, S. K. Oh, H. J. Kang, S. Heo, J. G. Chung, J. C. Lee, S. Tougaard, *Surf. Interface Anal.* **2012**, *44*, 623.

[34] C. Xiong, W. H. P. Pernice, H. X. Tang, *Nano Lett.* **2012**, *12*, 3562.

[35] W. Jin, R. G. Polcawich, P. A. Morton, J. E. Bowers, *Opt. Express* **2018**, *26*, 3174.

[36] L. Pavesi, D. J. Lockwood, *Silicon Photonics II: Components and Integration*, Springer, Berlin **2011**.

[37] I. L. Chistyi, I. L. Fabelinskii, V. F. Kitaeva, V. V. Osiko, Y. U. V. Pisarevskii, I. M. Sil'Vestrova, N. N. Sobolev, *J. Raman Spectrosc.* **1977**, *6*, 183.

[38] C. Mart, T. Kämpfe, R. Hoffmann, S. Eßlinger, S. Kirbach, K. Kühnel, M. Czernohorsky, L. M. Eng, W. Weinreich, *Adv. Electron. Mater.* **2020**, *6*, 1901015.

[39] S. Kirbach, K. Kühnel, W. Weinreich, presented at *2018 IEEE 18th International Conference on Nanotechnology (IEEE-NANO)*, Cork, Ireland, July **2018**.

[40] S. Abel, F. Eltes, J. E. Ortmann, A. Messner, P. Castera, T. Wagner, D. Urbonas, A. Rosa, A. M. Gutierrez, D. Tulli, P. Ma, B. Baeuerle, A. Josten, W. Heni, D. Caimi, L. Czornomaz, A. A. Demkov, J. Leuthold, P. Sanchis, J. Fompeyrine, *Nat. Mater.* **2019**, *18*, 42.

**ADVANCED
SCIENCE NEWS**

www.advancedsciencenews.com

**LASER
& PHOTONICS
REVIEWS**

www.lpr-journal.org

[41] J. G. Kremer, F. Eltes, P. Stark, D. Stark, D. Caimi, H. Siegwart, B. J. Offrein, J. Fompeyrine, S. Abel, *Nat. Photonics* **2022**, *16*, 491.

[42] R. Takei, S. Manako, E. Omoda, Y. Sakakibara, M. Mori, T. Kamei, *Opt. Express* **2014**, *22*, 4779.

[43] G. Gu, M. G, *Appl. Phys. Lett.* **2008**, *92*, 053305.

[44] Q. Gao, Y. Zhang, Y. Yu, F. Meng, Z. Liu, *IEEE J. Photovoltaics* **2018**, *8*, 710.

[45] P. Jiang, Q. Luo, X. Xu, T. Gong, P. Yuan, Y. Wang, Z. Gao, W. Wei, L. Tai, H. Lv, *Adv. Electron. Mater.* **2021**, *7*, 2000728.

[46] E. Timurdogan, C. M. Sorace-Agaskar, J. Sun, E. Shah Hosseini, A. Biberman, M. R. Watts, *Nat. Commun.* **2014**, *5*, 4008.

[47] Y. Sebbag, I. Goykhman, B. Desiatov, T. Nachmias, O. Yoshaei, M. Kabla, S. Meltzer, U. Levy, *Appl. Phys. Lett.* **2012**, *100*, 141107.

[48] Z. Ma, Z. Li, K. Liu, C. Ye, V. J. Sorger, *Nanophotonics* **2015**, *4*, 198.